Available online at www.sciencedirect.com
ScienceDirect
Journal of Catalysis 242 (2006) 309–318
JOURNAL OF CATALYSIS
www.elsevier.com/locate/jcat

Energetics of methane dissociative adsorption on Rh{111} from DFT calculations

Bouke S. Bunnik *, Gert Jan Kramer

Schuit Institute of Catalysis, Chemical Engineering and Chemistry, Eindhoven Technical University, P.O. Box 513, NL-5600 MB, The Netherlands

Received 28 March 2006; revised 9 June 2006; accepted 12 June 2006

Available online 25 July 2006

Abstract

We present DFT calculations of methane activation and CH_x ($x = 0$–3) adsorption at a Rh{111} surface and compare our results with data for other elements. The activation mechanism has similar energetics as found for other transition metal surfaces, where the first and last steps are the most difficult. On Rh{111}, the CH dehydrogenation barrier is the highest. The CH radical is also the most stable fragment. The barrier that we find for the first methane activation step on Rh{111} is relatively low, lower than expected from comparing it with that step on Ru{0001} [I.M. Ciobîcă, F. Frechard, R.A. van Santen, A.W. Kleyn, J.P.J. Hafner, J. Phys. Chem. B 104 (14) (2000) 3364–3369] or Ni{111} [R.M. Watwe, H.S. Bengaard, J.R. Rostrup-Nielsen, J.A. Dumesic, J.K. Nørkov, J. Catal. 189 (1) (2000) 16–30] in terms of the Brønsted–Evans–Polanyi relation. Therefore, methane is likely more easily activated on Rh{111} than on Ru{0001} or Ni{111}. Adsorption on Rh{111} in general favors hollow sites, but the energy differences between sites are often $<10\ \mathrm{kJ\,mol^{-1}}$.

Keywords: Density functional calculations; Methyl; Methylene; Methylidyne; Methane activation; Rhodium; Chemisorption; Brønsted–Evans–Polanyi

1. Introduction

The dissociative adsorption of hydrocarbons (and the reverse, the formation of hydrocarbons) is an important reaction step in many chemical processes, particularly in steam reforming and catalytic partial oxidation (CPO), in which a CO and H_2 gas mixture is formed. Depending on the specific reaction conditions, some metals will be better suited than others as catalysts. A common feature is that the best catalysts are the group VIII metals Ir, Ru, and Rh. For CPO, the most suitable catalysts are the 4d and 5d group VIIIB metals, whereas Ni and Ru are used for steam reforming.

The function of the catalyst in CPO is twofold [3]: first, to adsorb and activate the hydrocarbon, a particular challenge for methane; and second, to selectively oxidize to syngas rather than to fully oxidize on to CO_2 and H_2O.

Although several DFT studies have been done on methane activation, most of these are cluster calculations like, for example, the extensive study by Au et al. [4], which includes Rh{111}. These small clusters suffer from edge effects, however, which limits the accuracy of these results. Also, surface relaxations are precluded for clusters of this size, whereas, for example, Henkelman and Jónnson [5] demonstrated that such relaxations greatly influence the transition state geometry and energy. Thus, periodic-slab calculations are much better suited for this purpose. However, to the best of our knowledge, the set of metals studied is smaller for periodic-slab calculations of methane activation, namely Ni{111} [2,6], Ru{0001} [1], and Pt{110}(1×2) [7], but not Rh. Henkelman and Jónnson [5] only studied removal of only the first hydrogen, on Ir{111} while Michaelides and Hu [8] gave some energies for CH_x hydrogenation reactions on Pt{111}. Quite a few cluster studies have been done on adsorption of CH_x ($x = 0$–3) at group VIIIB closely packed surfaces as well. Kua et al. [9] performed a complete study of adsorption with clusters, but the limitations mentioned above apply here as well. Apart from the adsorption studies leading to the above activation mechanisms, these studies tend to focus on studying CH_3 (Cu{111} [10], Ni{111} [11], and Rh{111} [12,13]) or another CH_x fragment (e.g., [14]). In some studies, only a three-layer slab is used, with the

* Corresponding author.
E-mail address: bouke@sg10.chem.tue.nl (B.S. Bunnik).

0021-9517/$ – see front matter
doi:10.1016/j.jcat.2006.06.015

top surface layer the only one optimized to ease computational requirements. These measures may lower the adsorption energies, as shown recently by Xiao and Xie [13] for Rh{111} in a comparison of some of these studies. Therefore, methyl is well studied, but to the best of our knowledge no complete and accurate picture of CH_x adsorption on Rh{111} has been available in the literature until now.

The above considerations mean that even though Rh is an important catalyst candidate for CPO, there is only limited knowledge of methane activation on the metal. To counter this, here we present a minimum energy activation mechanism of methane by dissociative adsorption on Rh{111} obtained by density functional theory (DFT) calculations, dealing with the first function of the catalyst in CPO. We also discuss the CH_x adsorption energies and geometries on Rh{111}, because we need these data to construct the mechanism.

An important question that any reaction mechanism should answer is what is the slowest, and thus the rate-determining, step. For methane activation, likely candidates for the rate-determining step are the initial step and the last step [4]. The former case is where the first hydrogen is removed and a chemically adsorbed fragment is obtained. In the latter case, CH_x fragments will remain on the surface, which in turn can react to form species other than CO, such as carbon deposits that poison the catalyst. The literature suggests that the CH radical is indeed very stable on these surfaces and is very difficult to dehydrogenate. On Ru{0001} as well as on Ni, that last step is therefore concluded to be rate determining [1,2]. This is seen from most of the cluster calculations as well [4,9].

2. Model and computational details

We carried out ab initio density functional theory (DFT) periodic calculations with the Vienna ab initio simulation package (VASP, versions 4.4.5, 4.5, and 4.6) [15,16]. In this code, the Kohn–Sham equations are solved using the generalized gradient approximation (GGA) as proposed by Perdew and Wang [17] (PW91) to describe all exchange and correlation effects, with the free energy as a variational quantity.

We used the Vanderbilt-type ultra-soft pseudopotentials [18] the package provides [19] with plane wave basis sets with a kinetic energy cutoff (in the last optimization phase) of 400 eV, 50 eV higher than that required for the C, H, and CH_x species. We chose this because of a possible later inclusion of O atoms in the model.

We determined a lattice constant for Rh by fitting a Rose equation of state [20] to a set of DFT calculations with varying lattice constants. The size obtained was 3.850 Å, 1.2% larger than the experimental value of 3.803 Å [21].

Our model consists of a slab of 5 metal fcc{111}[1] layers with an adsorbate on both sides, leading to a p(2 × 2) adsorption structure with an inversion center due to the two-sided adsorption. Apart from the constraints due to this adsorbate geometry, no other symmetry constraint was imposed. This led to the optimization of two layers on each side with a fixed center layer. VASP always uses three-dimensional periodic boundaries; therefore, we used a supercell of length equivalent to 12 metal layers in the surface normal direction, 26.7 Å, creating 15.6 Å of vacuum between slabs to avoid interaction between them [1]. From the size of the supercell, we obtained a surface of 4 metal atoms with a coverage (Θ) of 0.25 ML, so that adsorbates were separated by a distance of about 5.4 Å. The isolated CH_x molecules, C and H, were calculated in a cubic box with edges of 10 Å.

The p(2 × 2) fcc{111} lateral supercell was sampled with a 5 × 5 × 1 k-points mesh generated via the Monkhorst–Pack procedure [23], leading to 13 irreducible k-points in the Brillouin zone. For better convergence of the number of k-points needed, we used the smearing method of Methfessel and Paxton [24] (with $k_BT = 0.2$ eV), to allow for partial occupancies around the Fermi energy. However, all reported energies were extrapolated to $k_BT = 0$ eV.

Parameters were checked to convergence to within 0.5 kJ mol^{-1}. The energies do not converge with respect to coverage, as both Ciobîcă et al. [1] and Bengaard et al. [6] showed. Instead, this size was chosen to present a useful coverage value with a real physical and chemical meaning. We also calculated adsorption energies in a larger p(3 × 3) supercell with a coverage of 0.11 ML and a 3 × 3 × 1 k-point mesh.

For the isolated gas-phase radicals CH_3, CH_2, and CH, we performed spin-polarized calculations. For the fragments on the Rh surface and the empty slab itself, we found that spin-polarized calculations did not change our results. This may be due to the double-sided adsorption that causes us to always have an even number of electrons (for p(2 × 2)). A previous study found that geometries are unchanged from this but that energies may be greatly affected [13].

All configurations, adsorption sites as well as transition states (TS), were optimized with the pseudo-Newton RMM-DIIS algorithm [25] from a candidate geometry until the forces were converged to within 0.01 eV Å^{-1} (16 μJ m^{-1}). For the adsorption sites, the geometries were first converged to within 0.1 kJ mol^{-1}. After that, the forces were usually already close to being converged. Ensuring that the forces were well converged allowed us to ascertain that we found stable points on the surface potential energy surfaces (PES). In addition, we calculated harmonic frequencies for all TS and most adsorption sites, which allowed us to determine whether we are at a maximum, at a minimum, or at a TS.

We used two different methods to obtain the candidate TS. In quite a few cases we succeeded in finding a good candidate by starting from the TS geometries of [1] on Ru{0001} and stepwise allowing more and more degrees of freedom (DOF) to be minimized while freezing some DOF of the ions active in the TS. In other cases, we used the nudged elastic band method [26–29] (NEB), as implemented by code provided on the website of Jónsson and coworkers [30]. NEB gives the maximum on a minimum energy path (MEP) between reactant and product, serving as the candidate structure for the TS. The method

[1] We, like Petersen et al. [22], prefer to use {111} instead of (111) to describe the whole set of fcc and hcp closely packed surfaces studied rather than only the (111) specific orientation out of the set.

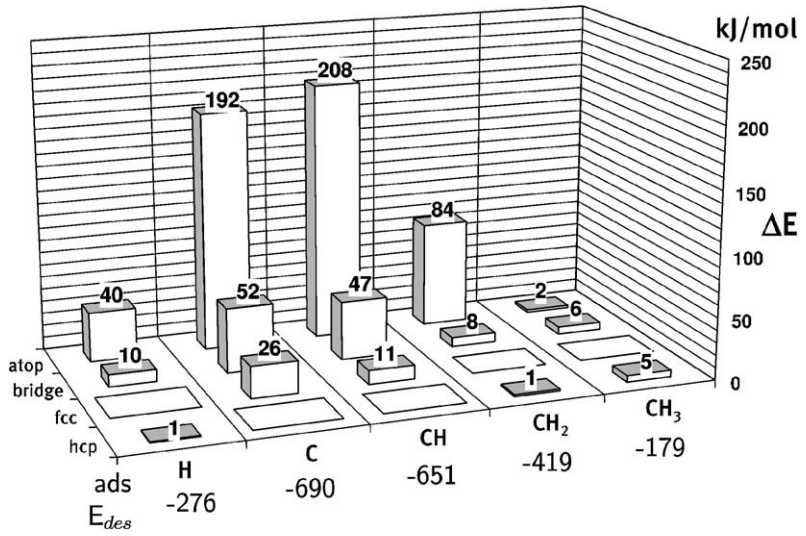

Fig. 1. Comparison of stability (kJ mol^{-1}) per adsorption site for all CH_x fragments ($x = 0$–3) and H. Below the graph we give the desorption energy for the most stable adsorption sites, the white squares that are at an energy of 0 kJ mol^{-1}. The height of the bars at the each site shows their higher energy compared to that minimum. Atop means that the fragment is adsorbed directly above an Rh atom, bridge is bridging between two Rh, hcp and fcc corresponds to adsorption at the two different hollow sites on the fcc{111} surface. Clearly, adsorption at hollow sites is preferred but for CH_3 the atop adsorption is a very close second.

approximates an MEP by taking intermediate images along the MEP. NEB efficiently minimizes the MEP, so that it is faster than step-by-step optimization. For a complicated mechanism, more images are required, but we found 4–10 to be sufficient.

3. Results and discussion

In this section we first describe and discuss the adsorption energies and geometries for H and all the CH_x ($x = 0$–3) fragments on Rh{111}. We also compare the stability of the products relative to methane. We then use those results and present an adsorption mechanism for methane, which is essentially the minimum energy path. After that, we go through the mechanism step by step from CH_4(g) to the final products, C and H adsorbed on the surface, describing the minimum energy transition-state geometries and energies.

For comparison of our results, we often refer to three sets of data, on Ru{0001} by Ciobîcă et al. [1,31], and Ni{111} by Watwe et al. [2], who presented complete reaction mechanisms like we do for Rh{111}, and Pd{111} by Paul and Sautet [32], who presented only adsorption data. For ease of reference, we drop the reference in the rest of the text. As mentioned in Section 2, the Ru{0001} calculations and the present study share most of the parameters and thus are well suited for a comparison, increasingly so because of the small difference in the lattice constants between Rh (3.850 Å) and Ru (3.818 Å [31]). The values used here for Ru{0001} differ slightly from those published previously; we refined the calculation of the gas-phase radicals and recalculated the results using the same gas-phase references as used for Rh{111}.

A limitation of the Ni{111} data is that the surface relaxations were not taken into account and that the calculations were not using spin polarization. Also, the two different threefold-hollow sites are grouped together without making a distinction.

3.1. Adsorption of CH_x and H

Fig. 1 schematically shows the desorption energies of the considered CH_x fragments and H, comparing the relative stabilities of the available sites; Table 1 gives the adsorption energies. The sites investigated are all high-symmetry sites of the closely packed surface. Atop adsorption is directly above a surface atom, bridge is bridging between two surface atoms, whereas the fcc and hcp sites are the two different threefold sites. They differ because hcp has a surface atom in the second layer, while fcc only has one in the third.

We see (Table 1) that in general our results agree reasonably with earlier slab calculations on Rh{111} [12,13,34]. The atomic fragments all favor hollow site adsorption. On Rh{111}, like on Cu{111} [10], Ru{0001} and Ni{111} slabs, the CH_x fragments also prefer hollow site adsorption. Pd{111} and Ir{111} [27], as well as Pt{111} [9] and other cluster calculations, do not follow that trend. Instead, for those metals, the most stable site maintains a fourfold-bonded carbon atom.

Combining the CH_x and H adsorption energies such that we have the same number of atoms as CH_4 (one CH_x and $(4 - x)$ H atoms), we can judge whether a reaction step is endothermic or exothermic with respect to methane in gas phase. We mention this for each fragment. In general, we see that Ni{111} and Pd{111} have a more endothermic methane activation than Ru{0001} and Rh{111}, as expected.

3.1.1. Carbon and hydrogen adsorption

Carbon is adsorbed in a hollow site, maximizing as expected its bonding to the surface. The hcp hollow site adsorption is the most stable. Adsorption at the fcc site is less stable, having a 26 kJ mol^{-1} lower desorption energy, for the bridge site adsorption that is 56 kJ mol^{-1}. Harmonic frequency analysis shows that atop adsorption is not a minimum but instead forms a second-order saddlepoint on the potential energy surface for

Table 1
Comparison of adsorption energies (kJ mol^{-1})[a]

System	Coverage (ML)	Source	CH_3^* fcc	CH_2^*	CH^*	C^*	H^* –
Rh	0.25	Current work	180.2 fcc	419.2 fcc	652.1 hcp	690.3 hcp	276.1 fcc
	0.11	Current work	180.9 fcc	421.5 hcp	661.4 hcp	705.1 hcp	275.1 fcc
Rh	1.0	[12][b]	−138.0 bridge	–	–	–	–
	0.33	[12]	220.0 fcc	–	–	–	–
	0.25	[34][c]	178 atop:s	–	–	686.0 hcp	269 fcc
		[13][d]	176.7 fcc	–	–	–	–
Ni	0.25	[2,6]	223 hollow	489 hollow	785 hollow	613 fcc	264 fcc
Cu	0.33	[10]	187.0 fcc	–	–	–	–
Ru	0.25	[31]	195.7 fcc	418.3 hcp	649.0 hcp	690.6 hcp	274.1 fcc
Ru	0.11	[31]	207.1 fcc	429.6 hcp	671.8 hcp	730.4 hcp	278.3 fcc
Pd	0.33	[32]	165 atop	353 bridge	569 hcp	617 fcc	225.8 –

[a] H is per adsorbed atom, H* (where * signifies adsorbed fragments). For comparing with the molecular gas, substract 220.5 kJ mol^{-1} per (1/2)H_2(g). The sites are the same as in Fig. 1, while hollow means hcp- or fcc-hollow was not specified. For CH_3^* the hollow site adsorption is always in the eclipsed configuration, as expected from the large energy difference with the staggered orientation.

[b] PBE functional, which in gives more accurate and slightly lower adsorption energies for two-atomic molecular adsorbates [33].

[c] Rh 3.83 Å, single sided adsorption on 3 layers of metal with only the top layer optimized.

[d] 5 metal layers, single-sided adsorption, spin-polarized.

carbon. The other three adsorption sites are minima, although the bridge site adsorption is a very shallow minimum. Diffusion of carbon always goes via bridge site adsorption. Because these are shallow, the diffusion transition state has an energy only slightly greater than the bridge site adsorption energy.

Compared with the literature, on Ru{0001} the sites are ordered in the same way; hcp hollow site adsorption is most stable, then adsorption at fcc (+40 kJ mol^{-1}), followed by bridge site adsorption (+57 kJ mol^{-1}). On Ni{111}, the two hollow sites are indistinguishable. On Pd{111}, the two hollow sites adsorption modes are indistinguishable as well, and bridge site adsorption is less stable (+67.5 kJ mol^{-1}). Other literature has reported that C is consistently adsorbed in the hcp hollow site, confirming our results. For adsorption at the hcp site, the C–Rh distance is 1.91 Å. The three atoms forming that surface site are pulled out of the surface, giving a corrugation of 0.12 Å.

For hydrogen, the adsorption energy $E_{ads,H} = 276.1$ kJ mol^{-1} is relative to the atomic H reference state, instead of the more common molecular H_2(g) reference state. This provides for an easier comparison with the other results in Table 1. Because the calculated H–H bond strength is 441 kJ mol^{-1} (E_{bind}), the adsorption energy from the molecule would be

$$2 \times 276 - 441 = 111.1 \text{ kJ mol}^{-1} \text{ } H_2(g),$$

or half that per H*.

Hydrogen is also adsorbed in a hollow site to maximize its bonding to the surface. Although hcp hollow site adsorption is the most stable, adsorption at the fcc site is less stable by the marginal amount of 1 kJ mol^{-1}. Bridge site adsorption is less stable by 10 kJ mol^{-1}. Harmonic frequency analysis shows that the bridge site adsorption is a First-order saddlepoint (a transition state), whereas atop site adsorption is a second-order saddlepoint on the potential energy surface for hydrogen. Adsorption at the hollow sites gives local minima. Diffusion of hydrogen, like that of carbon, occurs via bridge site adsorption. In this case, these sites are also the diffusion transition states. Compared with the literature reports, on all metals in Table 1 hollow site adsorption is the most stable. The energy difference between the adsorption at the two hollow sites is very small. For adsorption at the fcc site, the H–Rh distance is 1.86 Å. When adsorbed atop, this distance is considerably shorter (1.58 Å). The three atoms forming that surface site are pulled out of the surface slightly, giving a corrugation of 0.02 Å.

3.1.2. CH adsorption

For CH (methylidyne), the stable adsorption site is at the hcp hollow site. Adsorption at the fcc site is only 11 kJ mol^{-1} less stable. Bridge site adsorption is 47 kJ mol^{-1} less stable. Harmonic frequency analysis shows that the bridge site adsorption is a first-order saddlepoint (a transition state), whereas atop site adsorption is a second-order saddlepoint on the potential energy surface for methylidyne. The hollow site adsorptions are minima. Diffusion of methylidyne again goes via bridge site adsorption, the diffusion transition state. Compared with literature reports, on all metals in Table 1, methylidyne is adsorbed in the hcp hollow site. On Ru{0001}, fcc adsorption is 26 kJ mol^{-1}; on Pd{111} it is only 6 kJ mol^{-1} less stable. On Ru{0001}, bridge site adsorption is equally stable as on Rh{111} (42 kJ mol^{-1}); on Pd{111}, it is less stable (57 kJ mol^{-1}).

Fig. 2 shows the methylidyne adsorption geometry. The C–H bond length is similar to the gas-phase value. We checked that the minimum configuration indeed has the C–H bond perpendicular to the surface.

3.1.3. CH_2 adsorption

For CH_2 (methylene), the stable site is the fcc hollow site adsorption; hcp site adsorption is only 1 kJ mol^{-1} less stable, however. Bridge site adsorption is 8 kJ mol^{-1} less stable. Harmonic frequency analysis shows that bridge site adsorption is stable, whereas atop site adsorption is a second-order saddlepoint on the potential energy surface for methylene. Adsorption at the hollow sites again gives minima. Diffusion of methylene occurs via a transition state (4 kJ mol^{-1} higher than bridge) to a bridge adsorption site, then via a mirror transition state to the other hollow adsorption site. Compared with the other metals in Table 1, Ru{0001} has comparable energetics with hcp adsorption stable by 5 kJ mol^{-1} (vs fcc adsorption stable

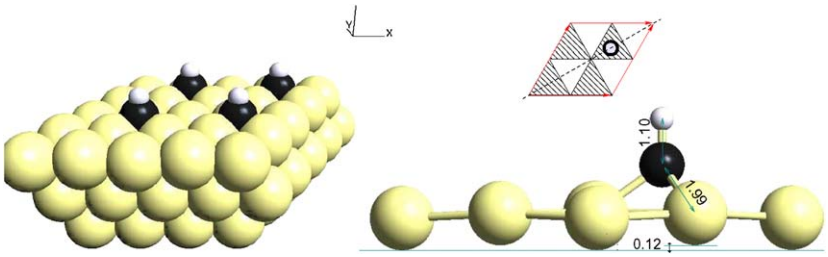

Fig. 2. The CH fragment has a very simple configuration, sitting in the middle of an hcp hollow site with the C–H bond perpendicular to the surface. CH inherits the threefold symmetry axes from the metal surface. The left panel gives an overview of the surface structure of the fragment. The top right panel is a schematic top-view of the surface unit cell, showing the hexagonal shape, with Rh atoms at the corner of each triangle (shaded: hcp, white: fcc). The dotted line shows the section used for the bottom right panel, where several relevant distances (Å) and angles (°) are given.

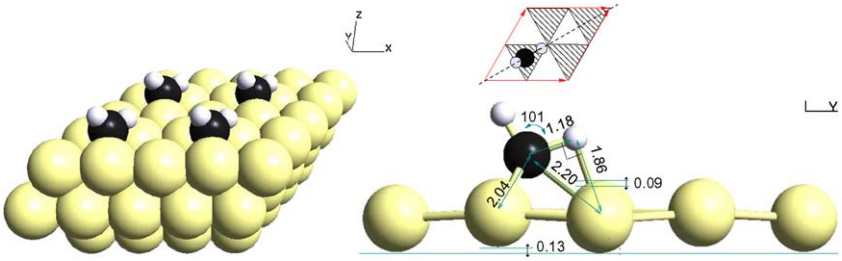

Fig. 3. CH_2 in its low energy configuration, on the hcp hollow site. The fcc geometry is almost the same. Here we show the hcp site as this is the start of the following de-hydrogenation step. For an explanation of the three panels in this figure, see Fig. 2. Note however that the CH system has the hcp and fcc sites swapped.

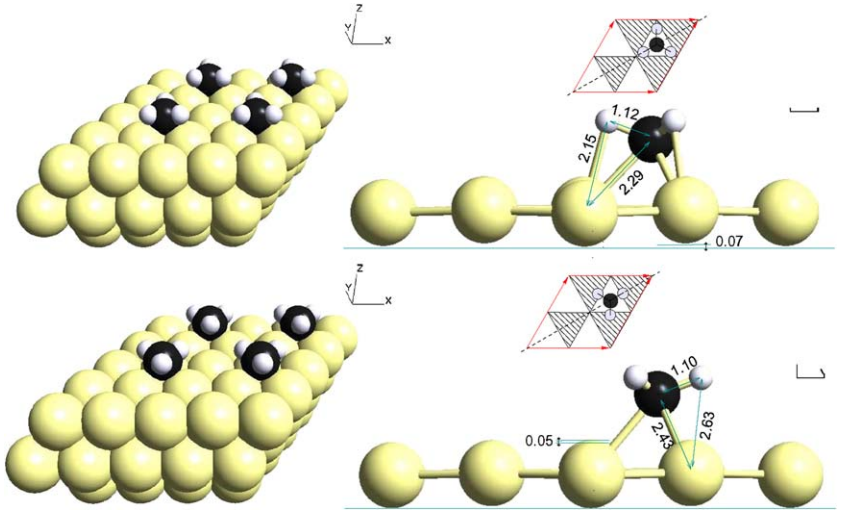

Fig. 4. Two configurations for CH_3. The top figure shows CH_3 in its most stable configuration in the fcc hollow site, with the surface Rh atoms "eclipsed" by the H atoms pointing towards them. The bottom figure shows CH_3 in the "staggered" configuration, rotated by 30° from eclipsed (bottom). The H atoms are further away from the Rh atoms, and the C atom in the center is also further away from the surface. Those differences lead to a 35 kJ mol^{-1} destabilization in this configuration. For an explanation of the three panels in those two figures, see Fig. 2.

by 1 kJ mol^{-1} for Rh{111}) and bridge adsorption less stable (22 vs 8 kJ mol^{-1}), whereas for Pd{111} and Pt{111} [8], bridge site adsorption is most stable and only then adsorption at the hollow sites. Fig. 3 shows the methylene low-energy adsorption geometry at the hcp site. Unlike the high-symmetry adsorption geometries described above, the CH_2 fragment is adsorbed asymmetrically in a hollow site. One C–H bond is elongated and almost parallel to the surface, with the hydrogen atom close to a Rh atom, whereas the other C–H bond points away from the surface and has a length similar to the gas-phase value. Notably, two rhodium atoms are pulled out of the surface by 0.13 Å. The fcc and hcp adsorption geometries match.

3.1.4. CH_3 adsorption

The CH_3 (methyl) fragment is most stable in an fcc-eclipsed geometry (see Fig. 4). The atop site is a close second (2 kJ mol^{-1}). The bridge site is the third most stable site (5 kJ mol^{-1}), whereas the hcp site is only slightly less stable (6 kJ mol^{-1}). With these small energy differences, diffusion of CH_3 on this surface should be easy. Compared with the other metals in Table 1, Rh{111} has smaller differences among all

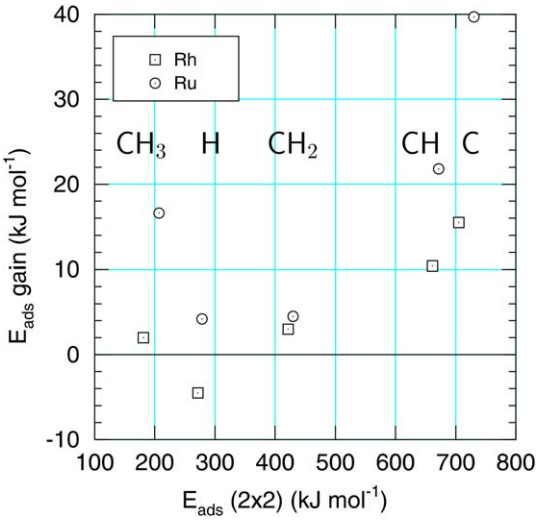

Fig. 5. Increase of adsorption energy for all considered CH_x fragments, C and H, when going from a p{2 × 2} to a p{3 × 3} structure, reducing the coverage from $\Theta = 0.25$ to 0.11 ML. The trends are the same for Ru{0001} and Rh{111}.

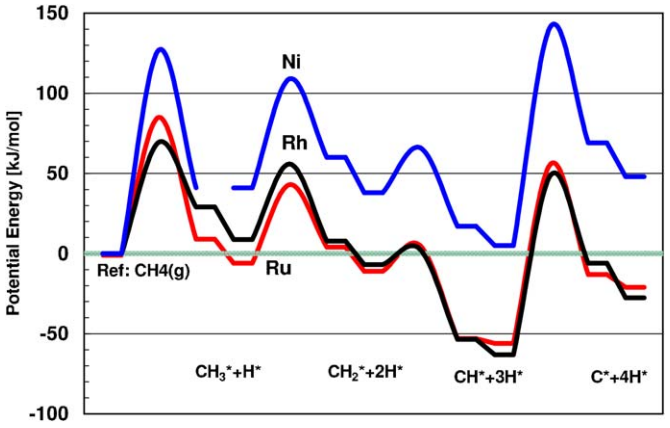

Fig. 6. Minimum energy paths for methane activation on Rh{111}, Ni{111} [2] and Ru{0001} [1]. Energies are in kJ mol^{-1} of adsorbed CH_4. We start with the reference of the empty slab and a CH_4(g). Right after each transition state we end with the co-adsorbed CH_x + H that is the product of the de-hydrogenation step. Then we continue with CH_x and H separately adsorbed. We end with C and H separately adsorbed at their most stable sites, hcp- and fcc-hollow. The Ni{111} dataset did not mention the CH_3 co-adsorption destabilization.

adsorption sites. On Ru{0001} and Ni{111}, the atop site is the least stable (+31 and +20 kJ mol^{-1}), followed by the bridge site (+17 kJ mol^{-1}). On Pd{111}, the atop site is the most stable (by 10 kJ mol^{-1}), followed by the hollow sites. The literature data on Rh{111} mostly agree with our findings; however, Robinson and Woodruff [10] reported that the atop site was considerably more stable than the hollow sites.

Fig. 4 shows the CH_3 fcc adsorption geometry. Two configurations are shown: two extrema of a rotation, with an energy difference of 35 kJ mol^{-1}. Notably, the atop site has a negligible energy change on rotation. This rotational effect is much bigger than the site dependency. We concur with Xiao and Xie [13] that Robinson and Woodruff [10] did not notice this effect, thus explaining the discrepancy.

3.1.5. Coverage dependency of adsorption

At higher coverages, we would expect destabilization due to repulsive interactions compared with low coverages. At very high coverages, we might even expect steric hindrance. The unstable adsorption of CH_x in the p{1 × 1} structure (Table 1) illustrates this. To investigate the influence of lower coverage, we calculated adsorption at the two most stable sites for all fragments with a lower coverage of $\Theta = 0.11$ ML, see Table 1. Fig. 5 shows the extra stabilization of the adsorbates due to the lower coverage for Rh{111} and for Ru{0001}.

With the p{2 × 2} adsorption structure, we found the following corrugations: CH: 0.12 Å, CH_2: 0.13 Å, C: 0.12 Å, CH_3: 0.07 Å and H: 0.02 Å. At lower coverage, the surface shows more corrugation (up to 0.14 Å, for CH and CH_2, C: 0.13 Å, CH_3: 0.08 Å and H: 0.04 Å) as the surface atoms binding to the adsorbates are pulled out of the surface, while most other atoms move inward. Note that the lower coverage is calculated in a larger system, which allows for such relaxations. We did not check the effect of a larger cell with the same coverage.

Fig. 5 shows that the stabilization seen on Rh{111} is much less than on Ru{0001}. The general trend of an increasing stabilization for higher adsorption energies and correspondingly higher surface corrugations is not surprising. The two lower points are H (even with decreased stability for Rh{111}) and CH_2. Interestingly, the stabilization of CH_2 is almost the same for Rh{111} and Ru{0001}. In both cases the corrugation is one of the largest, but the change is not so great. An interesting change for CH_2 is that for the low coverage situation, adsorption at the hcp site is favored by 4 kJ mol^{-1} over adsorption at the fcc site, which was the most stable at the higher coverage.

3.2. Minimum energy path for methane activation

Fig. 6 shows the minimum energy path (MEP) and compares it with the same path on Ru{0001} and on Ni{111}. After each step, we end up with a co-adsorbed CH_x and H. Then we start the next step with the CH_x and x individually adsorbed hydrogen atoms. This assumes that there are sufficient empty adsorption sites, and that diffusion of hydrogen is considerably faster than the dehydrogenation steps. The low diffusion barriers (Section 3.1.1 above) justify this assumption.

The MEP occurs via the most stable adsorption sites, CH_3^*(fcc) and CH_2^*(fcc), then a diffusion step to CH_2^*(hcp), and finishes via CH*(hcp), ending with a C*(hcp) and four H*(fcc) atoms. As mentioned above, the total reaction is 28 kJ mol^{-1} exothermic on Rh{111}, exothermic on Ru{0001} (+21 kJ mol^{-1}), and endothermic on Ni{111} and on Pd{111} (−41 and −72 kJ mol^{-1}, respectively). When converging the transition state, we identified numerous cases in which movement along 1 degree of freedom (DOF) showed only small energy increases. Because all of the transition-state geometries have a hydrogen atom close to a surface atom, it is interesting to note that the H–Rh distances are close to the value for H adsorbed atop (1.58 Å).

3.2.1. The $CH_4 \rightarrow CH_3^* + H^*$ reaction step

The transition state for the initial dehydrogenation step $CH_4 \rightarrow CH_3^* + H^*$ (Fig. 7) features an activated hydrogen atom

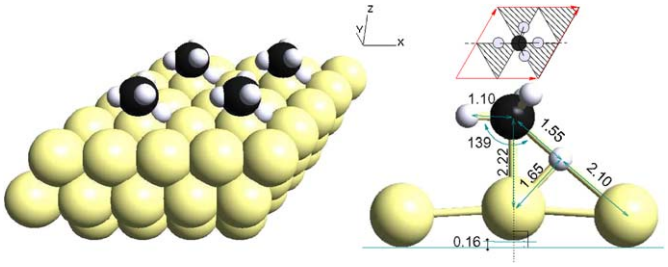

Fig. 7. Transition state for $CH_4 \rightarrow CH_3^* + H^*$. The activated C atom is almost exactly above a surface atom, with the activated C–H bond aligned along a bridge to the next Rh atom. For an explanation of the three panels, see Fig. 2.

close to one surface atom, with the remaining CH_3 moiety in a tilted atop position, almost unchanged from its configuration in the methane molecule. The central surface atom is pulled out of the surface by 0.16 Å. This geometry is similar to the transition state found on Ru{0001} and on Ir{111} [5]; only the carbon atom is, as reported, almost atop. We find a second transition state similar to that reported for Ni{111} and Pt{111} [8], but with an energy approximately 10 kJ mol^{-1} higher. Below we discuss the implications of this rather small difference.

The activation energy of 69.5 kJ mol^{-1} that we find for this step is considerably lower than on Ru{0001} (85.0 kJ mol^{-1}) and on Ni{111} (127.0 kJ mol^{-1}). Looking at Fig. 7, we see that the Rh and Ru transition state energies are switched around, considering that the methyl fragment is less stable on Rh{111} than on Ru{0001}. A reasonable explanation for this seems to be found in the fact that CH_3 is stable on atop for Rh{111}, in combination with the more atop transition-state geometry. The reaction $CH_4 \rightarrow CH_3^* + H^*$ (individually adsorbed) on Rh{111} is 8.7 kJ mol^{-1} endothermic. In contrast, the reaction is exothermic on Ru{0001} (+6 kJ mol^{-1}). On Ni{111} and on Pd{111}, the reaction is endothermic, however (+41 and +26 kJ mol^{-1}, respectively). Due to lateral interactions, the product of the reaction step, co-adsorbed methyl and hydrogen, is less stable (20.3 kJ mol^{-1}) than the separately adsorbed fragments. This is effect is larger than on Ru{0001} (18 kJ mol^{-1}). Such information is not available for Ni{111}.

3.2.2. The $CH_3^* \rightarrow CH_2^* + H^*$ reaction step

The transition state for $CH_3^* \rightarrow CH_2^* + H^*$ (Fig. 8) has a geometry not unlike the transition state found on Ru{0001} and on Ni{111}, but we feel that our geometry has a stronger asymmetry of the nonactivated CH_2 part of the transition state, which is already resembling the final CH_2^* geometry. The activation energy of 47.1 kJ mol^{-1} is about the same as on Ru{0001} (49.0 kJ mol^{-1}) and considerably lower than on Ni{111} (68.0 kJ mol^{-1}). As for Ru{0001}, the same reaction from the other hollow site, hcp adsorption, is less than 10 kJ mol^{-1} higher than this lowest activation energy.

The reaction $CH_4 \rightarrow CH_2^* + 2H^*$ (individually adsorbed) is 7 kJ mol^{-1} exothermic. On Ru{0001}, the reaction is also slightly exothermic (+11 kJ mol^{-1}). On Ni{111}, the reaction is endothermic (−38 kJ mol^{-1}). On Pd{111}, the reaction is also endothermic (−48 kJ mol^{-1}). Due to lateral interactions, the product of the reaction step, co-adsorbed methylene and hydrogen, is less stable than the above reaction by 15.0 kJ mol^{-1}, but less so than with methyl. On Ru{0001}, the effect is equally strong (15.0 kJ mol^{-1}), whereas on Ni{111}, the effect is even stronger (22 kJ mol^{-1}).

3.2.3. The $CH_2^* \rightarrow CH^* + H^*$ reaction step

The third transition state, for $CH_2^* \rightarrow CH^* + H^*$ (Fig. 9), is very similar to the stable CH_2 adsorption geometry (Fig. 3). This is a very easily reached transition state, consequently showing a very small activation energy of 9.5 kJ mol^{-1}, even lower than on Ru{0001} (16 kJ mol^{-1}). This barrier is so low

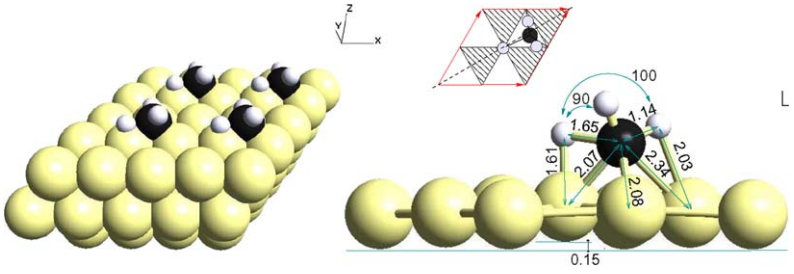

Fig. 8. Transition state for $CH_3^* \rightarrow CH_2^* + H^*$. The activated atom is again almost atop. Note the clear asymmetry, with the non-activated H atoms already close to their geometry in the product. For an explanation of the three panels, see Fig. 2.

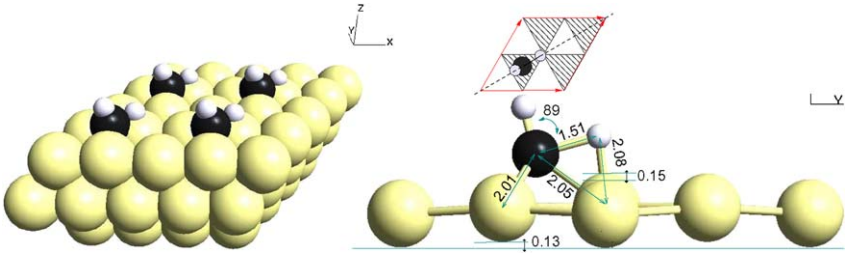

Fig. 9. Transition state for $CH_2^* \rightarrow CH^* + H^*$. The activated C–H bond is only slightly elongated from the CH_2^* stable geometry but the activated H atom is again almost atop. For an explanation of the three panels, see Fig. 2.

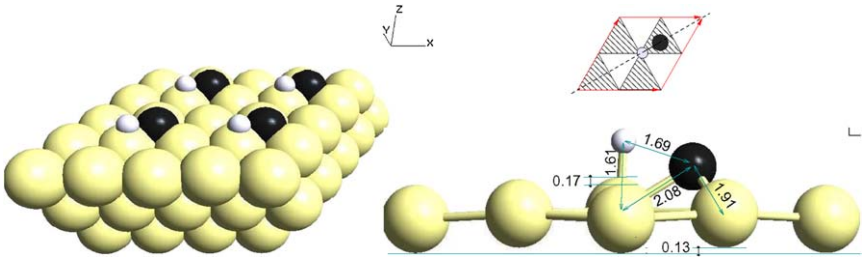

Fig. 10. Transition state for $CH^* \rightarrow C^* + H^*$. The activated C–H bond is almost parallel to the surface so that the H atom is again almost atop. For an explanation of the three panels, see Fig. 2.

that it competes with diffusion of CH_2. The Ni{111} transition state is similar in geometry but has an activation energy of 28 kJ mol^{-1}. Interestingly, the $NH + H \rightarrow NH_2 + H$ reaction on Pt{111} also has this geometry [8].

The reaction $CH_4 \rightarrow CH^* + 3H^*$ (individually adsorbed) is 63.1 kJ mol^{-1} exothermic. On Ru{0001}, this is also the case (+56.0 kJ mol^{-1}), but on Ni{111}, the reaction is slightly endothermic again (−5 kJ mol^{-1}). On Pd{111}, the reaction is endothermic (−39 kJ mol^{-1}). Due to lateral interactions, the products of the reaction step, co-adsorbed methylidyne and a hydrogen, are less stable than this, but by only a small amount (10.4 kJ mol^{-1}). On Ru{0001}, the effect is even smaller, 3.0 kJ mol^{-1}, whereas Ni{111} shows a similar value as on Rh{111} (12.0 kJ mol^{-1}). The energy gain from this reaction is by far the highest in the mechanism, 46.6 kJ mol^{-1}. Ru{0001} has a similar value (48 kJ mol^{-1}), whereas for Ni{111}, this is the only exothermic step (21 kJ mol^{-1}).

3.2.4. The $CH^* \rightarrow C^* + H^*$ reaction step

The transition state for the last step, $CH^* \rightarrow C^* + H^*$, has a quite different geometry than the previous steps, because the C–H bond is initially perpendicular to the surface but has to bend to be almost parallel to the surface in the transition state (Fig. 10). This explains why this barrier is so high on all of the surfaces compared. As demonstrated on Ni{111}, the activation energy for this step is significantly lowered on a stepped surface [6]. Michaelides and Hu [8] find a similar transition state for this reaction, and also for the N and O hydrogenation reactions on Pt{111}.

The overall reaction $CH_4 \rightarrow C^* + 4H^*$ (individually adsorbed) is 27.6 kJ mol^{-1} exothermic. Hydrogen is slightly more stable on Rh{111} than on Ru{0001} (276.1 vs 274.1 kJ mol^{-1}), so that on Ru the above reaction is only 21 kJ mol^{-1} exothermic, whereas the reaction is endothermic on Ni{111} (−48 kJ mol^{-1}) and even more for Pd{111} (−72 kJ mol^{-1}). Note that the Ni{111} heat of adsorption was indirectly derived using the hydrogen and carbon adsorption energies, but it does agree well with Fig. 6 in that paper.

Due to lateral interactions, the product of the reaction step, co-adsorbed carbon and hydrogen on Rh{111} is less stable than this by 21 kJ mol^{-1}. We see a similar value on Ni{111}, but on Ru{0001}, the effect is three times lower (8 kJ mol^{-1}).

3.2.5. The overall reaction

The overall reaction is exothermic on Rh{111}, which means that the combined adsorption energy of four hydrogen atoms and carbon is greater than the effect of breaking the four carbo–hydrogen bonds in methane. Due to the slightly higher adsorption energy of hydrogen on Rh{111} compared with that on Ru{111}, the reaction is slightly more exothermic on Rh{111} than on Ru{111}, despite carbon being clearly more stable on the latter metal.

Table 2
Summary of the C–H and C–Rh distances (in Å) of the transition state geometries discussed above (Section 3.2). The last column gives an indication of the relative "lateness" or "earliness" of the transition state that could be concluded from those distances

Step	C–H	H–Rh	
$CH_4 \rightarrow CH_3^* + H^*$	1.55	1.65	earlier
$CH_3^* \rightarrow CH_2^* + H^*$	1.65	1.61	later
$CH_2^* \rightarrow CH^* + H^*$	1.51	1.63	earlier
$C^* \rightarrow C^* + H^*$	1.69	1.61	later

In the first two steps, the driving force for dehydrogenation is small (negative and positive, respectively). The third step has a large positive driving force and a low activation energy, whereas the last step has a large negative driving force and a high activation energy. This makes the CH fragment a rather stable intermediate and a possible source of contamination of the surface.

Comparing with the other two metals in Fig. 6, Ru{0001} and Ni{111}, we see that this first step has a clearly lower activation energy on Rh{111}, whereas the other steps have a similar or lower barrier, so that the reaction should be faster on Rh{111} than on the other two metals, also due to the slightly higher exothermicity of the reaction.

3.3. Transition state geometries and the Brønsted–Evans–Polanyi relation

The Brønsted–Evans–Polanyi relation is shown to be generally applicable in catalysis [35]. It predicts a universal linear correlation between increases in energy gain (thermodynamics) and activation barriers (kinetics) for reactions with similar characters, independent of the catalyst used. The correlation factor α indicates whether a transition state has a geometry close to the reactant (α close to 0), or close to the product (α close to 1). Such transition states would be called early and late, respectively. Recently, Michaelides et al. [36] showed that on a range of transition metal surfaces the methane activation reaction steps all have the same correlation factor, which is close to 1, indicating that all transition states should be late. The

transition-state geometries found by Michaelides et al. [36] seem similar to ours, so that our results should agree with this. However, given our energy profile for the total reaction, we would expect the $CH_2^* \rightarrow CH^* + H^*$ reaction to have an early transition state and the first two steps to be neither early nor late. This would agree with observations on Ru{0001} [37, Section 4.3.6]. To study this further, we looked to a comparison of transition state geometries with the reactant and product geometries. Table 2 shows the C–H and H–Rh distances (with H the activated hydrogen atom) in the transition-state geometries. Looking at these distances, we see an interesting correlation, with the H–Rh distance shorter when C–H is larger. In the third column of the table, we conclude from this pattern that the first and third reaction steps should be relatively early compared with the second and last steps. The C–Rh distance decreases when we strip away hydrogen atoms (not shown); thus, this is not a decisive parameter here.

Looking at the reactant configurations, we see that in the stable adsorption sites, the C–H distance is a maximum of 1.18 Å (for CH_2). Furthermore, a hydrogen in CH_3 is 2.15 Å away from a surface atom. Comparing these values to those in Table 2 seems to point to late transition states; however, without a comparison to the reactant, this cannot be conclusively determined. But because in the product state the H and C are in different sites, the C–H distance is about 3.15–3.50 Å; based on this finding, we have to conclude that all transition states are earlier rather than later. Alternatively, we should perhaps not assume a linear correlation of C–H distance with lateness of the transition states. Thus this comparison does not finally answer our question.

There are other indications that assigning all of the different CH_x activation steps to a single class. As Fig. 6 shows, the activation energy of the first step is lower for Rh than for Ru, whereas the reaction is more endothermic on Rh. At the same time, the second step is more endothermic on Ru but has a slightly lower activation energy on Rh. In short, although our numbers do not preclude late transition states that would agree with the literature reports, they do indicate that the different CH_x steps do not all fall into the same class, in contrast to the universality curve of Michaelides et al. [36]. It seems the BEP relationship is an elusive one, warranting further study beyond the scope of this paper.

3.4. Limitations of the zero Kelvin minimum energy path approximation

For most adsorbed species, we saw a set of possible configurations with energies within or close to 10 kJ mol^{-1}, with low barriers for diffusion over the surface. In addition, several reaction steps seemed to have a set of transition states with energy differences in that same order. Considering the relevance of our work for the CPO reaction, which occurs at elevated temperatures, we note that at 1200 K, $k_B T = 11$ kJ mol^{-1}, comparable to the 10 kJ mol^{-1} energy differences. This means that the minimum energy path that we present here is probably a very good approximation of the true mechanism for CPO. Instead, the full mechanism should include paths, to some extent, those other configurations and reaction paths.

Note that although the results show the last step to have the highest activation energy, none of those results includes the zero-point energy (ZPE) of the gas-phase fragments or the effect of the extra degrees of freedom that the methane molecule in the gas phase. Those corrections would likely decrease the stability of all calculated adsorbed fragments, such that the first step could turn out to have the highest activation barrier. Because the energy differences are so small between some of the configurations, including this correction might also influence which site is more stable for which species.

Looking at the effect of lower coverage on adsorption, we would expect considerable stabilization of the transition states when going to such lower coverage. Indeed, as shown by Henkelman and Jónnson [5] for the first step in dehydrogenation on Ir (with an energy barrier of only 30 kJ mol^{-1}), and by Bengaard et al. [6] on Ni (with the energy barrier lowered to 101 kJ mol^{-1}), a larger supercell with more layers can considerably lower the transition state energy by allowing for very strong surface relaxation. The above reservations about the methodology used here led us to look in more detail at the kinetics and thermodynamics of the system. That work is the subject of undergoing calculations, which will be published later. Just adding a ZPE correction to our results does not change the minimum energy path picture much, due to the fact that the stronger contributions for each CH_x fragment (the high energy modes) remain mostly the same regardless of the adsorption site. Including more elaborate entropy effects would change this considerably, mainly because it would also lead to the need to include all, or at least many, pathways other then the MEP and take into account that we are dealing not only with vibrations, but also with (hindered) rotation modes. Here we confine ourselves to reporting on the MEP for methane activation. Finally, note that in the above we essentially work in a vacuum system, where the CH_4, H_2, or any other gas pressures are infinitely low. Also, we do not treat hydrogen dissociation, leaving the H coverage largely out of the picture. H recombination is expected to be (almost) barrierless. Including such effects, by taking into account the chemical potential of the gases, has become possible in recent years, but was not done here. Doing so would no doubt influence the relative stability of the different CH_x fragments in the reaction. An example of the expected effects is the case of preadsorbed H during the CH_4 activation step on Ru{0001} [1], where the TS remains unchanged but now the path has CH_3 temporarily at the atop site, whereas the two H atoms recombine before ending with CH_3 in a hollow site and a H_2 molecule in gas phase.

4. Conclusions and final remark

In this paper we have presented a detailed set of data on CH_x adsorption on Rh{111}. We found that hollow sites are the preferred adsorption sites. We also found that the atop site is a stable site for CH_3; for the other fragments, it is a second-order saddlepoint. The bridge site is stable for CH_3 and CH_2 and is a first-order saddlepoint otherwise. However, the energy differences between the sites are small, many within 10 kJ mol^{-1}, smaller than for other metals. Whether DFT can distinguish be-

tween sites with just a 1 or 2 kJ mol^{-1} difference in energy may be doubtful, but even if it cannot, the important factor to note is that many adsorption sites are very close in energy. Low diffusion barriers of, in particular, CH_2, H, and CH_3 imply a high mobility of these surface species.

With lower coverage, the adsorption energies increase. This increase is roughly proportional to the initial adsorption energy, although H and CH_2 are less stabilized than expected. The effect of co-adsorption of CH_x with hydrogen is destabilization due to lateral interactions between the two. On Rh{111}, this effect is larger than that on Ru{0001} but smaller than that on Ni{111}.

Taking the path via the most stable adsorption sites, we determined an MEP for stepwise methane activation on Rh{111}. The overall reaction is slightly exothermic, whereas the last two steps have the greatest change in energy over the step ($CH_2 \rightarrow CH + H$ exothermic, $CH \rightarrow C + H$ endothermic), so that the CH fragment is the most stable intermediate. The last step is both the most endothermic and has the highest activation energy. The first step has the second-highest activation energy excluding ZPE corrections (which would likely increase this value). The initial methane activation reaction has lower activation energy then expected when comparing the reaction heats and activation energies with those on Ru{0001} and Ni{111}. Although we find that our transition states might all be late, in agreement with recent literature, they should not all be equally late, and thus should not fit with a single correlation factor between activation energy and reaction heats. Our results indicate that a minimum energy path is perhaps a too-simple approximation of the full reaction mechanism for CPO, due to the small energy differences with other energy paths, in combination with the high temperature at which CPO occurs. Consequently, we have already started calculations to create a more complete thermodynamic and kinetic model of the reaction. Nevertheless, determining an MEP for this reaction on Rh{111} is an important first step toward a better understanding of the CPO reaction. It is also a useful and complete addition to our knowledge of methane activation on transition metal surfaces.

Acknowledgments

This study was sponsored by the Dutch Stichting Technische Wetenschappen (project UPC.5037). The authors thank Ionel Ciobîcă, Hiroshi Ohashi, and Rutger van Santen for providing access to their DFT results and for the fruitful discussions about those results and the parameters used in this study.

References

[1] I.M. Ciobîcă, F. Frechard, R.A. van Santen, A.W. Kleyn, J.P.J. Hafner, J. Phys. Chem. B 104 (14) (2000) 3364–3369.
[2] R.M. Watwe, H.S. Bengaard, J.R. Rostrup-Nielsen, J.A. Dumesic, J.K. Nørkov, J. Catal. 189 (1) (2000) 16–30.
[3] F. Zaera, Catal. Today 81 (2) (2003) 149–157.
[4] C.-T. Au, C.-F. Ng, M.-S. Liao, J. Catal. 185 (1) (1999) 12–22.
[5] G. Henkelman, H. Jónnson, Phys. Rev. Lett. 86 (4) (2001) 664–667.
[6] H.S. Bengaard, J.K. Nørskov, J. Sehested, B.S. Clausen, L.P. Nielsen, A.M. Molenbroek, J.R. Rostrup-Nielsen, J. Catal. 209 (2) (2002) 365–384.
[7] M.A. Petersen, S.J. Jenkins, D.A. King, J. Phys. Chem. B 108 (19) (2004) 5920–5929.
[8] A. Michaelides, P. Hu, J. Am. Chem. Soc. 122 (2000) 9866–9867.
[9] J. Kua, F. Faglioni, W.A. Goddard III, J. Am. Chem. Soc. 122 (10) (2000) 2309–2321.
[10] J. Robinson, D.P. Woodruff, Surf. Sci. 498 (3) (2002) 203–211.
[11] A. Michaelides, P. Hu, Surf. Sci. 437 (3) (1999) 362–376.
[12] E.J. Walter, A.M. Rappe, Surf. Sci. 549 (3) (2004) 265–272.
[13] H. Xiao, D. Xie, Surf. Sci. 558 (1–3) (2004) 15–22.
[14] A. Michaelides, P. Hu, J. Chem. Phys. 112 (13) (2000) 6006–6014.
[15] G. Kresse, J.P.J. Hafner, Phys. Rev. B 47 (1) (1993) 558–561.
[16] G. Kresse, J.P.J. Hafner, Phys. Rev. B 54 (16) (1996) 11169–11186.
[17] J.P. Perdew, Y. Wang, Phys. Rev. B 45 (23) (1992) 13244–13249.
[18] D. Vanderbilt, Phys. Rev. B 41 (11) (1990) 7892–7895.
[19] G. Kresse, J.P.J. Hafner, J. Phys.: Condens. Matter 6 (40) (1994) 8245–8257.
[20] J.H. Rose, J.R. Smith, F. Guinea, J. Ferrante, Phys. Rev. B 29 (6) (1984) 2963–2969.
[21] C.S. Barrett, T.B. Massalski, Structure of Metals, McGraw–Hill, New York, 2001.
[22] M.A. Petersen, S.J. Jenkins, D.A. King, J. Phys. Chem. B 108 (19) (2004) 5909–5919.
[23] H.J. Monkhorst, J.D. Pack, Phys. Rev. B 13 (12) (1976) 5188–5192.
[24] M. Methfessel, A.T. Paxton, Phys. Rev. B 40 (6) (1989) 3616–3621.
[25] P. Pulay, Chem. Phys. Lett. 73 (2) (1980) 393–398.
[26] G. Henkelman, G. Jóhannesson, H. Jónsson, in: Methods for Finding Saddle Points and Minimum Energy Paths, Kluwer Academic, London, 2000, pp. 269–300, chap. 10.
[27] G. Henkelman, H. Jónsson, J. Chem. Phys. 113 (22) (2000) 9978–9985.
[28] G. Henkelman, B.P. Uberuaga, H. Jónsson, J. Chem. Phys. 113 (22) (2000) 9901–9904.
[29] H. Jónsson, G. Mills, K.W. Jacobsen, in: Methods for Finding Saddle Points and Minimum Energy Paths, World Scientific, Singapore, 1998, pp. 385–404, chap. 16.
[30] H. Jónsson and coworkers, The Jónsson group VASP page, 2002–2004; http://www-theory.chem.washington.edu/vasp/.
[31] I.M. Ciobîcă, F. Frechard, R.A. van Santen, A.W. Kleyn, J.P.J. Hafner, Chem. Phys. Lett. 311 (3–4) (1999) 185–192.
[32] J.-F. Paul, P. Sautet, J. Phys. Chem. B 102 (9) (1998) 1578–1585.
[33] J.P. Perdew, K. Burke, M. Ernzerhof, Phys. Rev. Lett. 77 (18) (1996) 3865–3868.
[34] M. Mavrikakis, J. Rempel, J. Greeley, L.B. Hansen, J.K. Nørskov, J. Chem. Phys. 117 (14) (2002) 6737–6744.
[35] J.K. Nørskov, T. Bligaard, A. Logadottir, S. Bahn, L.B. Hansen, P.M. Bollinger, H. Bengaard, B. Hammer, Z. Sljivancanin, M. Mavrikakis, Y. Xu, P. Dahl, C.J.H. Jacobsen, J. Catal. 209 (2) (2002) 275–278.
[36] A. Michaelides, Z.-P. Liu, C.J. Zhang, A. Alavi, D.A. King, P. Hu, J. Am. Chem. Soc. 125 (13) (2003) 3704–3705.
[37] I.M. Ciobîcă, Ph.D. thesis, Eindhoven Technical University, 5600 MB Eindhoven, The Netherlands, Jan 2002; http://www.catalysis.nl/theory/publications/phdtheses.html.